

CFD simulation of the wind field over a terrain with sand fences: Critical spacing for the protected soil area

Izrael A. Lima^{a,b}, Eric J. R. Parteli^b, Yaping Shao^b, José S. Andrade Jr.^a,
Hans J. Herrmann^{a,c}, Ascânio D. Araújo^{a,*}

^a*Departamento de Física, Universidade Federal do Ceará, Fortaleza, 60451-970 Fortaleza, Ceará, Brazil*

^b*Department of Geosciences, University of Cologne, Pohligstr. 3, 50969 Cologne, Germany*

^c*Computational Physics, IfB, ETH Zürich, Schafmattstr. 6, 8093 Zürich, Switzerland*

Abstract

Sand fences are often erected to reduce wind speed and induce sand deposition and dune formation in areas affected by sand encroachment and desertification. However, the search for the most efficient array of fences by means of field experiments alone poses a challenging task given that field experiments are affected by weather conditions. Here we apply Computational Fluid Dynamic simulations to investigate the three-dimensional structure of the turbulent wind field over an array of fences of different sizes, porosity and spacing. We find that the area of soil protected against direct aerodynamic entrainment has two regimes, depending on the spacing L_x between the fences. When L_x is smaller than a critical value L_{xc} , the wake zones associated with each fence are interconnected (regime A), while these wake zones appear separated from each other (regime B) when L_x exceeds this critical value of spacing. The system undergoes a second order phase transition at $L_x = L_{xc}$, with the cross-wind width of the protected zone scaling with $[1 - L_x/L_{xc}]^\beta$ in regime A, with $\beta \approx 0.32$. Our findings have implication for a better understanding of aeolian transport in the presence of sand fences, as well as to develop optimization strategies for measures to protect soils from wind erosion.

Keywords: wind erosion, CFD, sand fences, soil protection

*Corresponding author

Email address: ascanio@fisica.ufc.br (Ascânio D. Araújo)

1. Introduction

Wind-blown sand is one important factor for the erosion of soils, the abrasion of rocks, the morphodynamics of ripples and dunes and the propagation of desertification. The most important transport mode of wind-blown sand grains is saltation, which consists of grains moving in nearly ballistic trajectories thereby ejecting new grains upon collision with the soil (splash) (Bagnold, 1941; Shao and Li, 1999; Almeida et al., 2006, 2008; Shao, 2008; Carneiro et al., 2011, 2013). The splash is also one of the main factors for the emission of dust (Shao et al., 1993; Shao, 2001; Lu and Shao, 1999), which, once entrained, may be transported over thousands of kilometers in suspension, thereby affecting climate and human health (Kok et al., 2012). Soil protection from aeolian erosion constitutes, thus, one aspect of broad implication for climate, environment and society.

To achieve aeolian soil protection, sand fences of various types are constructed with the aim at reducing wind velocity and inducing sand accumulation and dune formation (Li and Sherman, 2015; Gillies et al., 2017). Such fences typically consist of wire, lightweight wood strips or perforated plastic sheets attached to regularly spaced stakes (Pye and Tsoar, 1990). Moreover, most sand fences are porous, as solid fences that completely block the wind may induce strong vortices extending up to several fence heights downwind, while a porous fence protects larger areas of leeward sheltered ground than its solid counterpart does (Cornelis and Gabriels, 2005; Bruno et al., 2018).

However, the properties of three-dimensional turbulent wind flow over an array of fences are still poorly described. Their understanding is important to accurately predict wind erosion patterns in the presence of sand fences and to develop efficient strategies to protect sediment soils from aeolian erosion. While most of the previous investigations (Baltaxe, 1967; Wilson, 1987; Lee and Kim, 1999; Lee et al., 2002; Wu et al., 2013; Dong et al., 2006; Telenta et al., 2014; Zhang et al., 2015; Tsukahara et al., 2012; Savage, 1963; Nordstrom



Figure 1: Application of sand fences to prevent wind erosion — a field example. The image shows fences made of coconut leaves in Paracuru, near Fortaleza, main city of State of Ceará in Northeastern Brazil (photo by first authors, I.A.L. and A.D.A.).

et al., 2012; Telenta et al., 2014; Hatanaka and Hotta, 1997; Alhajraf, 2004; Wilson, 2004; Bouvet et al., 2006; Santiago et al., 2007; Liu et al., 2014; Bitog et al., 2009) focused on the flow characteristics over a single fence, it has been shown by means of wind-tunnel experiments (Guan et al., 2009), as well as Computational Fluid Dynamic simulations (Lima et al., 2017), that large-scale arrays consisting of many fences (5-10 fences or more) exhibit larger wind speeds near the ground between fences far downwind in the array. Moreover, the simulations by Lima et al. (2017), which calculated the average turbulent wind flow in a two-dimensional cut along the symmetry axis of the fences, showed how maximal wind speeds occurring within the array depend on fence porosity, spacing and height. However, to more realistically model scenarios with fences of finite cross-wind width, three-dimensional simulations are required.

In the present work, we simulate the turbulent flow over a three-dimensional array of sand fences. Our aim is to investigate how the total area of the soil that is protected against wind erosion depends on the main parameters of the system, i.e. fence porosity, height and spacing. To define this area, we consider the average wind velocity close to the ground within the region between the fences. We want to provide useful insights e.g. for developing strategies to optimize the design of an array of fences. One of the challenges in such strategies consists

in achieving maximal soil protection with the smallest amount of material for fence construction and maintenance (Lima et al., 2017). In this manuscript, we thus provide comparative results from simple arrays of fences (i.e. when the fence height and inter-fence spacing are constant over the field) with those from complex arrays of fences with multiple values of height and spacing.

2. Numerical experiments

Figure 2 shows the schematic representation of the setup employed in our simulations. This consists of a three-dimensional channel of height $\Delta z = 10 h_f$, width $\Delta y = 20 h_f$ and length $\Delta x = 80 h_f + 9L$, while the fences, each of height h_f , are erected vertically on the bottom wall of this channel at different values of inter-fence spacing L , as described later. The fences have a cross-wind width $W_f = 10 h_f$, which is 50% of the lateral width Δy of the wind channel (Fig. 2). The soil level in the absence of the fences is constant and equal to zero, while the dimensions of the wind channel are chosen to be large enough to ensure that border effects can be neglected, but small enough for efficient numerical simulation. We have checked that the results, presented in the next section, remained unchanged by increasing the box dimensions.

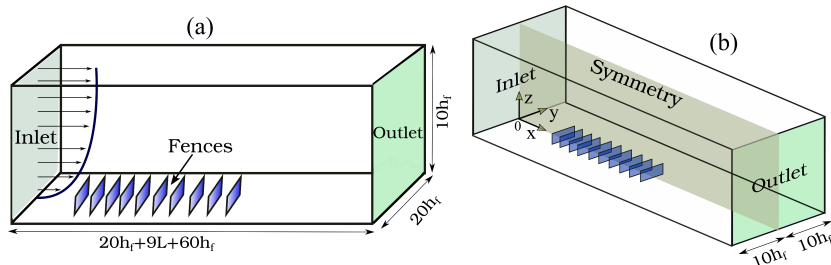


Figure 2: Schematic diagram showing the geometry of the wind channel with the array of fences on its bottom. The fences have height h_f and between them a spacing L . At the inlet, the logarithmic profile for the wind velocity is imposed following Eq. (1).

We consider that the fences are subjected to an average turbulent wind flow in x direction (cf. Fig. 2). In the absence of fences, the average horizontal wind

velocity over the flat ground $\vec{u}(x, y, z)$ increases logarithmically with the height z above the bed level (Bagnold, 1941; Pye and Tsoar, 1990). To represent such average upwind flow condition in our calculations, the logarithmic velocity profile for $\vec{u}(x, y, z)$ is imposed as boundary condition at the simulation inlet. Specifically, at the horizontal position $x = 0$, $\vec{u}(0, y, z) = 0$ for $z = \delta$, where δ is the surface roughness. The horizontal velocity increases with z according to the following equation (which is valid for $z \geq \delta$) (Bagnold, 1941; Pye and Tsoar, 1990):

$$\vec{u}(0, y, z) = \frac{u_{*0}}{\kappa} \log\left[\frac{z}{\delta}\right] \vec{e}_x, \quad (1)$$

where \vec{e}_x is the unit vector pointing in the direction x , u_{*0} is the magnitude of the upwind shear velocity of the wind and $\kappa = 0.4$ is the von Kármán constant. The shear velocity u_{*0} is proportional to the mean flow velocity gradient in turbulent boundary layer flow, and is used to define the upwind shear stress,

$$\vec{\tau}_0 = \vec{\tau}(0, y) = [\rho_{\text{air}} u_{*0}^2] \vec{e}_x, \quad (2)$$

where $\rho_{\text{air}} = 1.225 \text{ kg/m}^3$ denotes the air density. Moreover, we take for the surface roughness the value $\delta = 100 \mu\text{m}$, which is within the range between $10 \mu\text{m}$ and 1.0 mm valid for dune fields (Pye and Tsoar, 1990).

In our calculations, each sand fence is modeled as a vertical, porous wall, implemented by a special type of boundary condition representing a porous membrane of a certain velocity/pressure drop characteristics (Wilson, 1985; Santiago et al., 2007; Araújo et al., 2009; Yeh et al., 2010). At height z , this pressure drop is given by the expression

$$\Delta p(x, y, z) = -\frac{1}{4\Phi^2} \rho_{\text{air}} [\vec{u}(x, y, z) \cdot \vec{e}_x]^2 \Delta m, \quad (3)$$

where the term in the brackets is the wind velocity normal to the fence, i.e. the horizontal wind speed at height z , Δm is the fence's thickness and Φ its porosity. The fences' thickness is set as $\Delta m = 10^{-4} \text{ m}$, while a nominal porosity of 20% (Li and Sherman, 2015; Lima et al., 2017) is used in our calculations.

We consider that the fluid (air) is incompressible and Newtonian, while the calculation of the average turbulent wind field over the soil is performed as de-

scribed in previous works (Herrmann et al., 2005; Araújo et al., 2013). Specifically, the Reynolds-averaged Navier-Stokes equations are solved using the FLUENT Inc. commercial package (version 14.5.7), in which the standard $\kappa-\epsilon$ model is applied in the computations to simulate turbulence. The time-averaged (or Reynolds-averaged) Navier-Stokes equations for the wind flow over the terrain are solved in the fully-developed turbulent regime. In the calculations, a non-slip boundary condition is applied to the fluid-solid interface defined by the soil and the fences, while at the top wall, the shear stress of the wind is set equal to zero (Herrmann et al., 2005; Almeida et al., 2006, 2008; Araújo et al., 2013; Michelsen et al., 2015; Lima et al., 2017). Since the fences have a finite crosswind width $W_f = 0.5 \cdot \Delta y$ (see Fig. 2), to avoid border effects and to resolve the flow in the region around the edges of the fences, both edges of the fence array are separated from the lateral walls by a distance equal to half the fence width (see Fig. 2). Given the symmetry of the system, and for the sake of computational efficiency, a symmetric boundary condition is applied in the y direction, with symmetry plane $y = 0$. The flow equations are, thus, solved for the right half of the simulation domain, and the developed solution mirrored along the symmetry plane $y = 0$ to obtain the flow field on the left half. Both lateral walls are treated as full slip walls, i.e. having zero shear stress.

Moreover, the default pressure-velocity coupling scheme (“SIMPLE”) of the solver, which obtains a correction in the static pressure field such as to satisfy the continuity equation (Patankar and Spalding, 1972), is applied with its preselected values of parameters. At the outlet, a static pressure $P = 0$ is specified, while the default option “standard wall functions” of the solver is selected (Araújo et al., 2013; Lima et al., 2017). This option applies the wall boundary conditions to all variables of the $k - \epsilon$ model that are consistent with Eq. (1) along the channel’s bottom wall (Launder and Spalding, 1974).

To perform the calculations, a second-order upwind discretization scheme is applied to the momentum, whereas for the turbulent kinetic energy and turbulence dissipation rate we apply a first-order upwind scheme (Araújo et al., 2013). A rectangular grid with mean spacing of about 0.05 m is used for the lower re-

gion from the bottom wall ($z = 0$) up to the height of the fences ($z = h_f$), while for larger heights, a coarser grid is considered. Specifically, the grid cell size is 0.10 m within the range $h_f \leq z < 2h_f$ and 0.50 m for $2h_f < z \leq 10h_f$ (i.e. up to the top wall).

Moreover, the following initial conditions are applied: for all values of x, y, z , the velocity and the pressure are set to zero, while at the left wall ($x = 0$), the logarithmic profile Eq. (1) is imposed. Convergence of the numerical solution of the transport equations is evaluated in terms of residuals, which provide a measure for the degree up to which the conservation equations are satisfied throughout the flow field. Here, convergence is achieved when the normalized residuals for both ϵ and k fall below 10^{-4} , and when the normalized residuals for all three velocity components (in the directions x, y and z) fall below 10^{-6} .

3. Results and discussion

Fig. 3 shows flow streamlines over an array of 10 fences of height $h_f = 0.5$ m, spacing $L_x = 20 h_f = 10$ m and porosity $\phi = 20\%$. Moreover, the cross-wind width of the fences is $W_f = 5$ m. The wind velocity upwind of the fences, u_{*0} , is 0.4 m/s, and its direction is indicated by the arrow in Fig. 3. The streamlines shown in this figure clearly indicate the increase in the internal boundary layer due to the presence of the fences, which has been discussed previously from two-dimensional CFD simulations considering the two-dimensional cut along the symmetry line of the fences (Lima et al., 2017) (see also Guan et al. (2009); Jerolmack et al. (2012)). Here, in the three-dimensional simulation shown in Fig. 3, we see that the flow between the first two fences is recirculating in the lateral direction (y) with very small wind velocities (a), which is in contrast to the situation of the last downwind pair of fences (c) where the highest wind speeds occur and the referred whirls are not observed.

3.1. Longitudinal profile of the wind shear velocity near the surface

We calculate, for different longitudinal slices of the system, i.e. slices in the direction of the wind, the wind shear velocity $u_{*x}(x, y)$ as a function of the

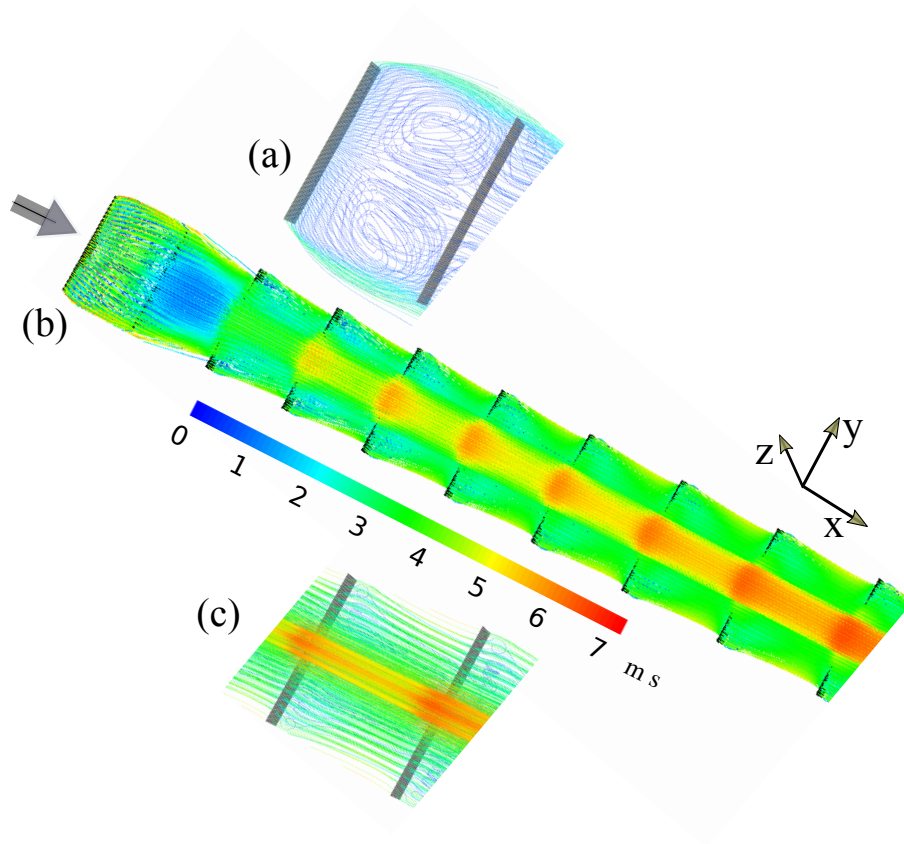


Figure 3: Streamlines of the average turbulent wind flow over an array of 10 fences. The colors indicate the magnitude of the wind velocity in m/s. The result for all fences is shown in (b). In (a) we see the streamlines for the first and second fences, while the streamlines for the last two fences in the array are shown in (c). The arrow at left in (b) indicates the wind direction. Upwind shear velocity of the wind is 0.4 m/s, fence porosity is 20% and fence height is 50 cm, while fence spacing is 5 m.

downwind position x close to the ground. Following the experimental work by Guan et al. (2009), we use the relation

$$u_{*x}(x, y) \approx u_{*0}r(x, y), \quad (4)$$

where the two-dimensional field $r(x, y)$ is defined as $r(x, y) \equiv u_x(x, y, z = 0.2 h_f)/u_x(0, y, z = 0.2 h_f)$, with $u_x(x, y, z) = \vec{u}(x, y, z) \cdot \vec{e}_x$ denoting the longitudinal component of the wind velocity. $r(x, y)$ gives thus the attenuation in the longitudinal wind velocity due to the presence of the fences, computed at a height of $z = 0.2 h_f$ above the soil at the position (x, y) . By doing so, we obtain the results shown in Fig. 4, which correspond to the same parameter values of the simulation in Fig. 3.

We see in Fig. 4 that the wind shear velocity in the region between the fences near the symmetry axis of the system ($y = 0$) is reduced by a substantial amount. In particular, between the last two fences in the system, the maximal value of u_{*x} at $y = 0$ is about 63% of the upwind shear velocity u_{*0} , while the wind shear velocity increases with the lateral position towards the flanks of the fences. The two uppermost curves in Fig. 4 correspond to values of $|y| > 2.5$ m, that is beyond the lateral borders of the fences. We see that in this outer region, the wind shear velocity is largest thereby exceeding the upwind value u_{*0} after the third fence. This result can be understood by noting that the fence array imposes an obstacle for the wind, and that there is thus a pressure reduction at the lateral border of the fence array. This pressure reduction is associated with the conservation of momentum of the fluid flow in the system, which leads to an increase in wind velocity near the flanks of the fence array.

Moreover, we see in Fig. 5 that the behavior of u_{*x} along the flanks of the fence array depends on the fence porosity ϕ . The increase in flow velocity at the lateral borders is stronger the higher the porosity, since the pressure drop at the sides of the fence array is stronger the less permeable the fences.

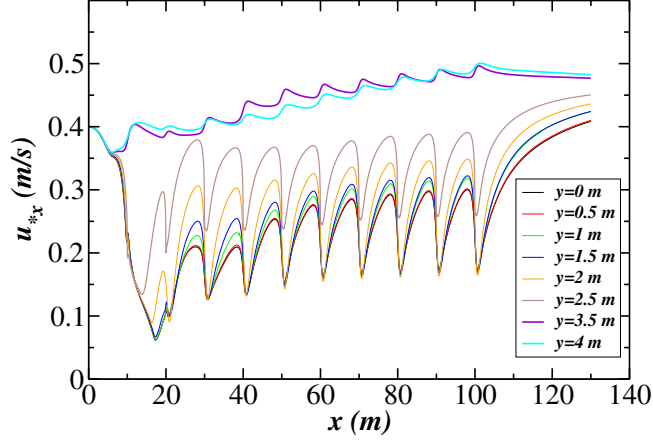


Figure 4: Average longitudinal component of the wind shear velocity, u_{*x} , calculated using Eq. (4), as a function of the downwind position x for different values of y . The first fence is at $x = 10$ m, the last one at $x = 100$ m and the spacing is $L_x = 10$ m. Fence porosity is 40%, fence cross-wind width is 5 m and fence height is 50 cm, while the upwind shear velocity is $u_{*0} = 0.4$ m/s.

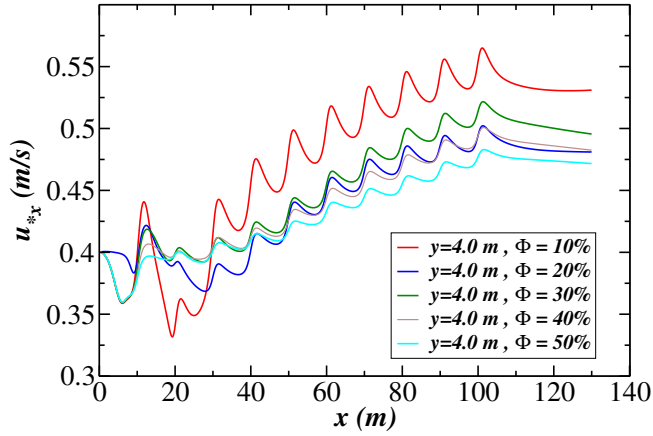


Figure 5: Average longitudinal component of the wind shear velocity, u_{*x} , calculated using Eq. (4), as a function of the downwind position x for $y = 4$ m and different values of porosity ϕ . Fence positions and sizes are as in Fig. 4. Moreover, the upwind shear velocity is $u_{*0} = 0.4$ m/s.

3.2. Area protected against sand transport

One important aspect of a sand fence array is its efficiency to protect soil against motion of sand grains. Since the impact of sand particles on the ground during saltation causes dust emission (Shao et al., 1993), soil protection against sand transport has implications not only for the dynamics of sand encroachment and aeolian desertification, but also for the Earth’s climate and atmosphere.

Fig. 6 shows the two-dimensional field of the longitudinal component of the wind shear velocity close to ground as a function of the horizontal position, $u_{*x}(x, y)$. The blue area in the figure represents the wake region within the fence array, i.e. values of $u_{*x}(x, y)$ smaller than 0.25 m/s, which is approximately the minimal threshold shear velocity for direct entrainment of sand particles by fluid forces (Bagnold, 1941). We see in Fig. 6 that the shape of the wake region changes with distance downwind. For the first upwind fences, wake zones produced by the adjacent fences appear connected to each other, but they disconnect after the fourth fence.

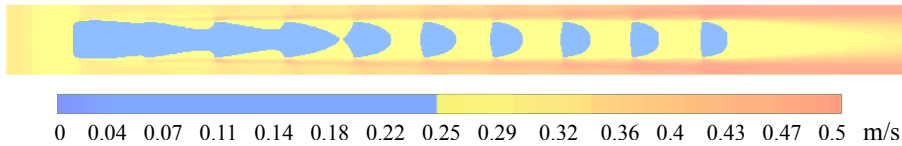


Figure 6: Longitudinal component of the wind shear velocity field, u_{*x} , calculated using Eq. (4), for the array of fences in Fig. 4. The colors indicate the values of u_{*x} in m/s.

Moreover, the shape of the wake zones as a function of the downwind distance, as well as the downwind position where the wake zones separate from each other, depend on several parameters of the system, such as upwind flow velocity u_{*0} , inter-fence distance L_x , fence porosity ϕ and number of fences in the array. Figure 7 shows how the wake zones depend on the spacing between the fences. This figure shows that, for $u_{*0} = 0.4$ m/s, $\phi = 20\%$ and 10 fences, separation of the different wake zones of the fences starts after a certain value of spacing which is within the range $15 < L_x/h_f < 20$.

We investigate this behavior in more detail by varying the fence porosity

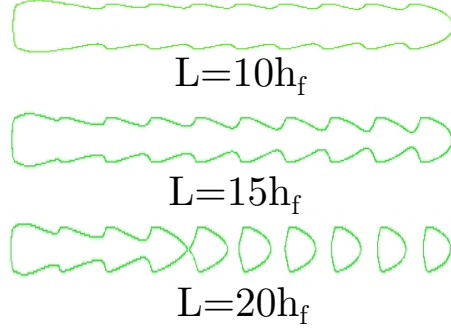


Figure 7: Contour plot of the protected soil area, i.e. the area within which $u_{*x} < u_{ft}$ ($= 0.25$ m/s), for different spacings between the fences. The other parameters are the same as in Fig. 4.

and spacing (see Figs. 8a-c). The fence height is constant and equal to 50 cm, while the upwind flow shear velocity is 0.4 m/s (Lima et al., 2017). Each one of Figs. 8a-c shows the total protected area S , for which $u_{*x} < u_{ft}$ ($= 0.25$ m/s), as a function of the fence number $\#i$. This area S is measured from the mid positions between the two neighbouring fences, that is,

$$S = \int_{-0.5 \Delta_y}^{0.5 \Delta_y} \int_{x_i - 0.5 L_x}^{x_i + 0.5 L_x} \Theta(u_{*x}(x, y) - u_{ft}) \cdot dx dy \quad (5)$$

where $\Theta(x)$ is the Heaviside function, i.e. $\Theta(x) = 0$ for $x \leq 0$ and unity otherwise, while Δ_y is the cross-wind width of the channel and L_x the fence spacing.

For a spacing of $10 h_f$ (Fig. 8a), we see that, for all porosity values from 10% to 50%, the wake region consists of interconnected wake zones forming a protected soil region of approximately constant shape and size throughout the fence array. This behavior leads to an approximately constant value of S associated with each fence, although for very high porosities the flow through the last fences tends to recover upwind conditions earlier, thus leading to a drop in the value of S . By taking a larger value for the fence spacing (cf. Fig. 8b; $L_x = 15 h_f$), the fence wake zones appear inter-connected in the beginning of the array (up to the fourth fence). We see that, in this initial region, the value of S is approximately the same for all values of porosity (see Fig. 8b). However, from

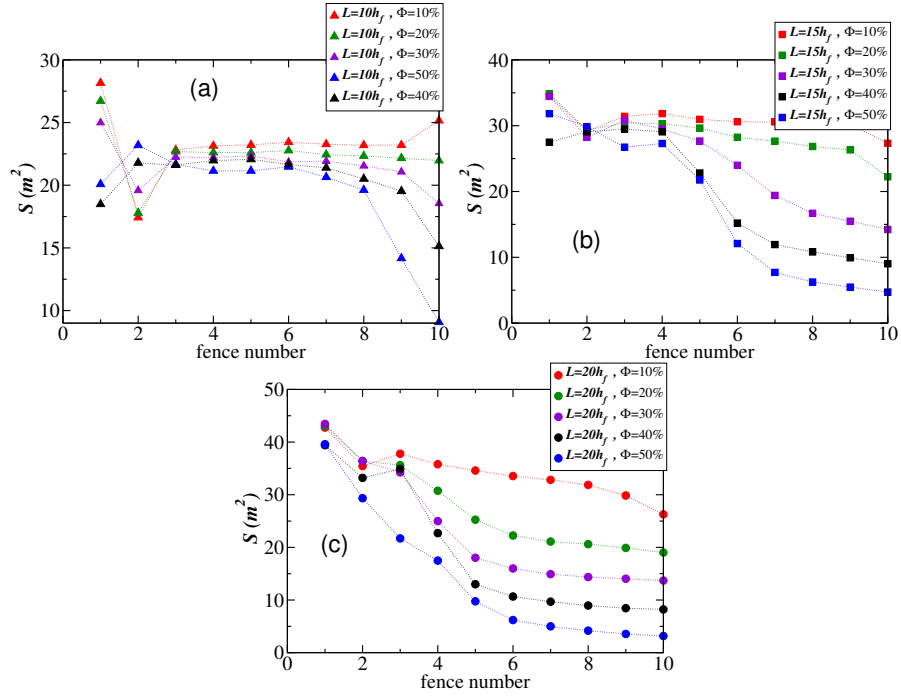


Figure 8: Protected soil area S between two adjacent fences, i.e. the area within which $u_{*x} < u_{ft}$ ($= 0.25$ m/s), as a function of the fence position downwind for different values of the spacing and porosity. The area S is defined according to Eq. (5) and is rescaled by $S_0 = \Delta_y \cdot L$, which is the area between two adjacent fences.

the fourth fence onwards, the zones of shear velocity below threshold become smaller due to the obstacle’s permeability, and S starts to decrease downwind at a rate that increases with fence porosity. This behavior is associated with a thinning of the wake region with distance downwind as can be seen in Fig. 7).

Moreover, Fig. 8b shows that, for high enough porosities, S first decreases rapidly with distance downwind (between fences 4 and 6) and then slowly from the sixth fence onwards, thus indicating the approach to an asymptotic value for very large downwind distances. This asymptotic behavior corresponds to the regime of disconnected wake zones, which is achieved faster the larger the fence spacing (see Fig. 7). Furthermore, we calculate in Fig. 8c the value of S as a function of the fence position for a higher spacing of $20 h_f$. Clearly, the spacing in these calculations is so large that a dependence of S on the porosity is observed from the very beginning of the array, i.e. S decreases faster downwind the larger ϕ . The separation of the wake zones produced by the fences occurs from the sixth fence onwards for all values of ϕ larger than 10%. Far downwind within the array, the system is found within the regime (or phase) of separated / disconnected wake zones (regime B), which is separated from the upwind regime of inter-connected wake zones (regime A) at some point within the array depending on the inter-fence spacing.

3.3. Two-fences experiments elucidate the critical dependence of wake zones connectivity on inter-fence spacing

To investigate the dependence of the wake zones between adjacent fences on the spacing, described above, we perform systematic calculations of the protected soil area between an isolated pair of fences for different values of spacing. To this end, we perform a different type of numerical experiments in which only 2 fences are considered, while the spacing between both fences is systematically varied. The two fences have the same height, porosity and cross-wind width as the fences in the array considered in the previous calculations. Moreover, the wind tunnel has the same height and width Δy , and boundary conditions are the same as before. The only difference compared to the setup of Fig. 2 is the

channel's downwind length, which is now $80h_f + L$.

Figure 9 shows the contour plot of the wake zone from the upwind fence including the entire protected area associated with the downwind fence. In this particular calculation, the porosity is 40%, the fence height is 50 cm, the spacing is $10h_f$ and the upwind shear velocity is 0.4 m/s.

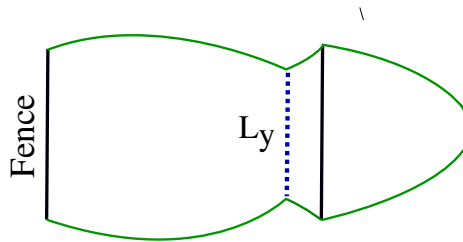


Figure 9: Contour of the area S protected against aeolian entrainment in the two-fences experiment, obtained for $u_{*0} = 0.4$ m/s, $h_f = 50$ cm, $\phi = 40\%$ and $L_x = 20h_f$ (spacing). L_y denotes the smallest cross-wind width of the protected region between the fences.

In Fig. 9, L_y denotes the smallest cross-wind width of the wake zone between the two fences. This cross-wind width decreases with the fence spacing L_x as shown in Fig. 10. We see from this figure that there is a critical value of L_x/h_f , which is slightly larger than 34, beyond which L_y is zero, i.e. the wake zones of the two fences are separated from each other. For larger values of the spacing ($\tilde{L}_x \equiv L_x/h_f \gtrsim 34$), the system is in the disconnected phase (regime B; $\tilde{L}_y \equiv L_y/h_f = 0$), while as the spacing decreases ($\tilde{L}_x \lesssim 34$), the system enters regime A, i.e. the connected phase ($\tilde{L}_y \neq 0$).

This behavior is similar, for instance, to the transition of percolation from the connected to the disconnected phase as the probability p that a site in the graph is open decreases below a critical value p_c (Herrmann and Roux, 1990; Stauffer and Aharony, 1994; Bunde and Havlin, 1996; Araújo et al., 2002; Parteli et al., 2010). In other words, in the system of Fig. 10, the cross-wind width of the wake zone between the fences, L_y , goes to zero with a power law at $\tilde{L}_x = \tilde{L}_{xc}$ around 34 from regime B to regime A. We can thus describe the behavior of \tilde{L}_y by means of the following equation,

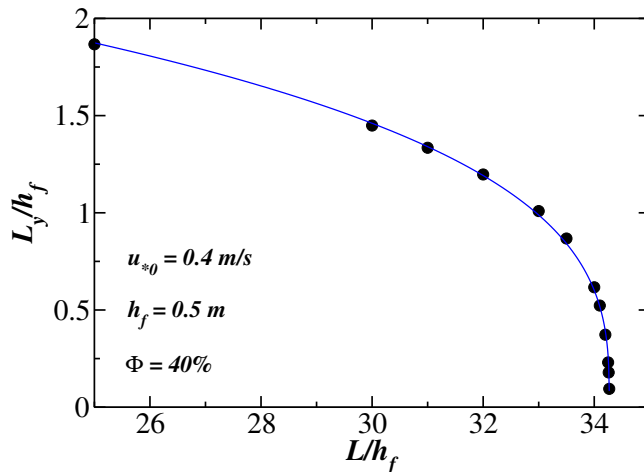


Figure 10: Value of L_y defined in Fig. 9 as a function of the spacing between the fences, L_x , in the two-fences experiment. Both L_y and L_x are normalized by the fence height h_f . The filled circles denote our calculation data. The continuous line represents the best fit using Eq. (6), which gives $\tilde{L}_{xc} \approx 34.3$, $A \approx 2.85$ and $\beta \approx 0.32$.

$$\tilde{L}_y = \begin{cases} A \cdot \left[1 - \tilde{L}_x/\tilde{L}_{xc}\right]^\beta, & \tilde{L}_x < \tilde{L}_{xc} \\ 0, & \tilde{L}_x \geq \tilde{L}_{xc} \end{cases} \quad (6)$$

where the critical point \tilde{L}_{xc} , the constant A and the exponent β can be determined from the best fit to the simulation data. The continuous line in Fig. 10 shows this best fit, which gives $\tilde{L}_{xc} \approx 34.3$, $A \approx 2.85$ and $\beta \approx 0.32$. The quality of the fit is remarkable. We thus conclude that the change in the system's behavior from regime A to regime B exhibits the characteristics of a second order phase transition at the critical spacing \tilde{L}_{xc} , where \tilde{L}_y represents an appropriate observable (order parameter) to describe this transition.

The results of our simulations are important for the drag partitioning schemes in models for aeolian surfaces with sand fences. In regime B, i.e. $\tilde{L}_x > \tilde{L}_{xc}$, the total drag can be then partitioned into a pressure drag, due to the momentum absorbed by the individual fences, and the surface drag on the underlying surface (Raupach, 1992). However, in regime A, i.e. $\tilde{L}_x < \tilde{L}_{xc}$, interactions of the

turbulent wakes and mutual sheltering among the fences (see Fig. 7) lead to a reduction in the pressure drag on individual fences. In other words, as the density of the roughness elements increases, individual elements become less effective since only a fraction of them can be seen by the mean flow (Shao and Yang, 2005; Yang and Shao, 2006). As shown by Shao and Yang (2005), the effect of mutual sheltering between the roughness elements can be taken into account by including in the drag partitioning scheme by Raupach (1992) a third component, which is the skin drag due to momentum transfer to the surfaces of roughness elements (Shao and Yang, 2005; Yang and Shao, 2006).

However, it is interesting to discuss the disconnection of the wake zones between two adjacent fences within an array (cf. Fig. 7) in the light of the analysis made for two isolated fences in Figs. 9 and 10. For a fence array, we have found that the wind shear velocity is increasing downwind, which means that \tilde{L}_y decreases with distance downwind. The larger the spacing of the array, the earlier within the array the transition from regime A to regime B (disconnected wake zones) will occur, which means that the wind shear velocity is one important parameter controlling the critical spacing \tilde{L}_{xc} . However, the analysis presented here represents a first step towards a complete description of the complex behavior of the protected soil area as a function of the geometric properties of an array of sand fences.

3.4. Multiple or constant fence heights?

In this subsection, we address the question whether combining fences of different heights may increase the efficiency of the fence array. Using the same amount of fence material, the aim is to find a combination of fence heights for which soil protection against aeolian erosion is optimal. To characterize soil protection, we consider the total amount of protected area (S) and we analyze different configurations of fences using two different heights, namely $h_f = 50$ cm and $h_f = 1$ m, defined as follows:

- setup A — fences of height $h_{f1} = 1.0$ m separated by a distance $10h_{f1}$ (= 10 m)

- setup B — fences of height $h_{f1} = 1.0$ m separated by pairs of fences of height $h_{f2} = 50$ cm, with constant spacing 6.67 m between all fences (see Fig. 11)
- setup C — fences of height $h_{f1} = 1.0$ m separated by pairs of fences of height $h_{f2} = 50$ cm, with spacing determined by the height of the upwind fence — in this setup, each pair of adjacent fences within the array is separated by a distance equal to 10 times the height of the upwind fence
- setup D — fences of height $h_{f2} = 50$ cm separated by a distance $10h_{f2}$ ($= 5$ m)

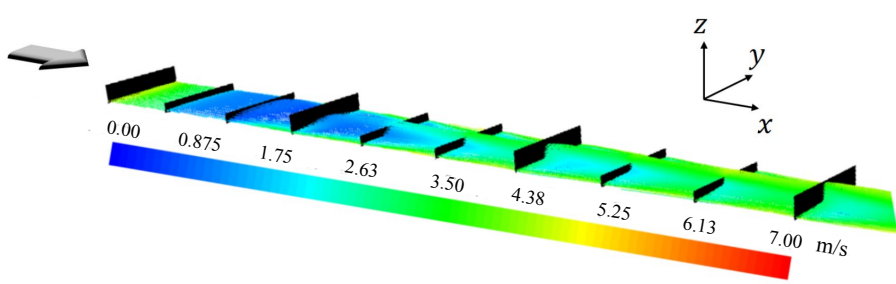


Figure 11: Flow streamlines obtained for setup B, i.e. fences of height 1 m separated by pairs of fences of height 50 cm with constant spacing 6.67 m. The colors indicate the magnitude of the wind velocity in m/s. Upwind flow velocity $u_{*0} = 0.4$ m/s and fence porosity $\phi = 40\%$.

Figure 12 shows the two-dimensional velocity field of the horizontal wind shear velocity $u_{*x}(x, y)$ for setups A-D, by using a fence porosity of 40% and upwind shear velocity 0.4 m/s. The total area S for which $u_{*x} < u_{ft}$ is calculated, as described in the previous subsection, as a function of the downwind position for all setups, and the result is shown in Fig. 13. In this figure, the protected area produced by each fence is shown rescaled by the total area S_0 between the fence and its downwind neighbour. We can see that setup D, which uses constant fence height of 50 cm, produces larger values of S/S_0 compared to setup A (constant fence height of 1 m). Moreover, this figure shows that setups using multiple fence heights lead to intermediate efficiency between the two investigated setups of

constant fence height. Nevertheless, we see that, at some positions along the array, setups B and C locally produce lower S/S_0 than setup A and higher S/S_0 than D, and the efficiency of the array should be thus analysed by considering an average over the entire surface on which the fences have been erected.

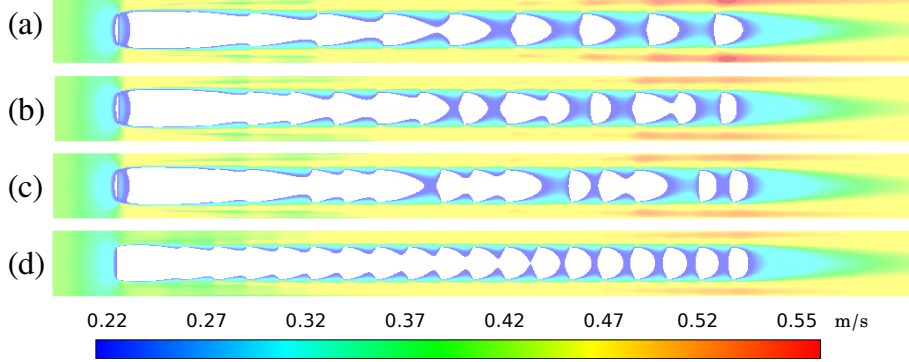


Figure 12: Longitudinal component of the wind shear velocity field, u_{*x} , for the arrays of fences of setups A-D using multiple fence heights. The colors indicate the values of u_{*x} in m/s. The calculation results correspond to upwind flow velocity $u_{*0} = 0.4$ m/s and fence porosity $\phi = 40\%$, while fence height and inter-fence spacing are varied over the different setups as described in Section 3.4.

We see in Fig. 12 that the unprotected soil zones in the different setups ($u_{*x} > u_{ft}$) display very distinct behaviour with respect to the distribution of wind shear velocities. In particular, the “gaps” between the wake zones in setup A are larger thus giving rise to higher transport rates between the fences in setup A than in setup D. We thus expect that using setup A may lead to larger transport rates compared, for instance, to setup D. To verify this behavior, we calculate the following quantity for the different setups,

$$Q = \int_{-0.5 \Delta_y}^{0.5 \Delta_y} \int_{10}^{100} \Theta(u_{*x}(x, y) - u_{ft}) \cdot [u_*^2(x, y) - u_{ft}^2] dx dy \quad (7)$$

which determines, up to a pre-factor encoding parameters related to sediment and fluid properties, the saturated sediment flux with the wind shear velocity (Lettau and Lettau, 1978; Kok et al., 2012). More precisely, we calculate the ratio Q/Q_0 for all setups, where Q_0 is given by Eq. (7) with $u_*(x, y) = u_{*0}$, that

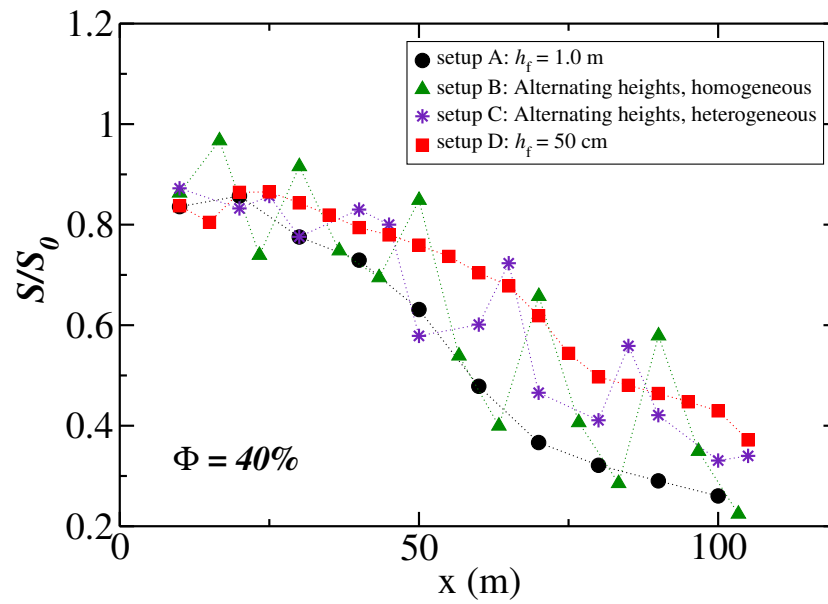


Figure 13: Area S of soil between adjacent fences protected against aeolian entrainment as a function of the downwind position, computed for the different setups A-D using multiple fence heights. The points in each curve correspond to the fences $i = 1 \dots N$ in the respective setups A-D, while S is the protected area between fence i and $i + 1$, i.e. the area between the adjacent fences within which $u_{*x} < u_{*ft}$. Moreover, S_0 represents the total area $\Delta_y \cdot L_i$ between fences i and $i + 1$.

is the undisturbed wind shear velocity in the absence of the dunes. We note that the sand flux in Eq. (7) incorporates important simplifications, in particular neglecting the hysteresis in sediment transport — i.e. the correct threshold wind velocity in the flux equation would be the impact threshold, which is about 80% of u_{ft} (Bagnold, 1941; Kok et al., 2012). Moreover, Eq. (7) also neglects the effect of the saturation length of sediment transport on the downwind relaxation of the flux toward its saturated value (Sauermann et al., 2001; Kroy et al., 2002). Nevertheless, the present analysis is useful to investigate the trend in the transport rate with respect to the fence array setups defined above.

Our calculations yield the results given in Table 1. Clearly, setup D performs best with respect to sand flux reduction. That an array of fences of constant height 50 cm performs better than 1.0 m has been suggested before from two-dimensional CFD simulations that neglect lateral transport, although the present three-dimensional calculations show that this better performance is related to a larger reduction in the transport rates.

Table 1: Sand flux reduction due to sand fences arranged according to the different setups. The sand flux in the presence of the fences has been calculated using Eq. (7), while Q_0 denotes the sand flux without the presence of the fences ($u_{*x} = u_{*0} = 0.4$ m/s throughout the field).

setup	A	B	C	D
Q/Q_0	0.120	0.074	0.083	0.052

We have also investigated the average wind shear velocity within the disturbed boundary layer in the region above the fences, i.e. at height between $3 h_f$ and $8 h_f$ (Guan et al., 2009). Within this region, wind shear velocities are larger than u_{*0} throughout the array of fences, with the speedup decreasing downwind towards an asymptotic value (Guan et al., 2009; Jerolmack et al., 2012). However, to the best of our knowledge, our study is the first systematic investigation of the two-dimensional field $u_x(x, y)$ associated with the near-surface wind shear velocity on the protected soil. We hope that the present study will motivate future investigation on the effect of different system parameters on the protected area S , as well as on the critical rescaled distance \tilde{L}_{xc} , the constant A

and the exponent β in Eq. (6). Moreover, it would be interesting to verify our prediction for the phase transition in Eq. (6) by means of field measurements or wind tunnel experiments.

4. Conclusions

We performed three-dimensional CFD simulations of the average turbulent wind field over a flat terrain in presence of an array of porous fences. The calculations were performed with different values for porosity, height and spacing, and the present work focused on the total area of sediment soil protected against aeolian entrainment. We found that there is a critical inter-fence spacing L_{xc} that separates two regimes of behavior: For $L_x > L_{xc}$, the wake zones of the different fences in the array are disconnected (regime B), while for $L_x < L_{xc}$, no separation occurs between zones of wind shear velocity below threshold (regime A). We find that the system undergoes a continuous phase transition from regime B to regime A as L_x decreases below L_{xc} . In regime A, the cross-wind width of the protected zone, L_y (the order parameter) scales with $(1 - L_x/L_{xc})^\beta$, where the exponent β is around 0.32.

One outlook of the present work would be the simulation of the soil topography in presence of the fences. Such simulations can be achieved by coupling the CFD modeling presented here with the morphodynamic model for aeolian landscapes developed in the last years (Sauermann et al., 2001; Kroy et al., 2002; Sauermann et al., 2003; Parteli et al., 2006; Herrmann et al., 2008; Durán et al., 2010; Parteli et al., 2011; Luna et al., 2009, 2011, 2012; Melo et al., 2012; Parteli et al., 2014).

Moreover, many open questions remain to be investigated in the future, such as how the predictions reported here change if intermittent transport conditions that occur in real field scenarios (Ellis et al., 2012; Sherman et al., 2013) are considered. Moreover, one further aspect to be incorporated in future studies is the effect of the stochastic nature of turbulence on the threshold for sand and dust emission. Accurately modeling such forces is a difficult task that is still

matter of intense research (Klose and Shao, 2012), and is important to correctly represent threshold wind speeds for sediment entrainment (Kok et al., 2012; Li et al., 2014). Large-scale arrays of sand fences disposed in different ways, such as in zig-zag (Bitog et al., 2009) or checkerboards (Qiu et al., 2004), should be also modeled in future works. Finally, we hope that the predictions made from the simulations presented here will trigger field work to verify our results, as well as further effort toward optimization of strategies to protect soil erosion with sand fences.

Acknowledgements

This work was supported in part by CAPES, CNPq and FUNCAP (Brazilian agencies), the Brazilian Institute INCT-SC, by the German Research Foundation (DFG) Grant RI 2497/7-1 and by ERC Advanced grant FP7-319968 FlowCCS of the European Research Council.

References

References

- Alhajraf, S., 2004. Computational fluid dynamic modeling of drifting particles at porous fences. *Environ. Model. Softw.* 19, 163–170.
- Almeida, M.P., Andrade Jr., J.S., Herrmann, H.J., 2006. Aeolian transport layer. *Physical Review Letters* 96, 018001.
- Almeida, M.P., Parteli, E.J.R., Andrade Jr., J.S., Herrmann, H.J., 2008. Giant saltation on Mars. *Proceedings of the National Academy of Sciences* 105, 6222–6226.
- Araújo, A.D., Andrade Jr., J.S., Maia, L.P., Herrmann, H.J., 2009. Numerical Simulation of Particle Flow in a Sand Trap. *Granul. Matter* 11, 193–200.

- Araújo, A.D., Moreira, A.A., Makse, H.A., Stanley, H.E., Andrade Jr., J.S., 2002. Traveling length and minimal traveling time for flow through percolation networks with long-range spatial correlations. *Physical Review E* 66, 046304.
- Araújo, A.D., Parteli, E.J.R., Pöschel, T., Andrade Jr., J.S., Herrmann, H.J., 2013. Numerical modeling of the wind flow over a transverse dune. *Scientific Reports* 3, 2858.
- Bagnold, R.A., 1941. *The physics of blown sand and desert dunes*. Methuen, London.
- Baltaxe, R., 1967. Air Flow Patterns in the Lee of Model Windbreaks. *Arch. Meteorol. Geophys. Bioklimatol. Ser. B* 15, 3.
- Bitog, J.P., Lee, I.B., Shin, M.H., Hong, S.W., Hwang, H.S., Seo, I.H., Yoo, J.I., Kwon, K.S., Kim, Y.H., Han, J.W., 2009. Numerical simulation of an array of fences in Saemangeum reclaimed land. *Atmos. Environ.* 43, 4612–4621.
- Bouvet, T., Wilson, J.D., Tuzet, A., 2006. Observations and Modeling of Heavy Particle Deposition in a Windbreak Flow. *J. Appl. Meteorol. Clim.* 45, 1332–1349.
- Bruno, L., Fransos, D., Lo Giudice, A., 2018. Solid barriers for windblown sand mitigation: Aerodynamic behavior and conceptual design guidelines. *Journal of Wind Engineering & Industrial Aerodynamics* 173, 79–90.
- Bunde, A., Havlin, S., 1996. *Fractals and Disordered Systems*. Springer, Berlin-Heidelberg.
- Carneiro, M.V., Araújo, N.A.M., Pächtz, T., Herrmann, H.J., 2013. Mid-air collisions enhance saltation. *Physical Review Letters* 111, 058001.
- Carneiro, M.V., Pächtz, T., Herrmann, H.J., 2011. Jump at the onset of saltation. *Physical Review Letters* 107, 098001.
- Cornelis, W.M., Gabriels, D., 2005. Optimal windbreak design for wind-erosion control. *J. Arid Environ.* 61, 315–332.

- Dong, Z., Qian, G., Luo, W., Wang, H., 2006. Threshold velocity for wind erosion: the effects of porous fences. *Environ Geol.* 51, 471–475.
- Durán, O., Parteli, E.J.R., Herrmann, H.J., 2010. A continuous model for sand dunes: Review, new developments and application to barchan dunes and barchan dune fields. *Earth Surf. Proc. Landforms* 35, 1591–1600.
- Ellis, J.T., Sherman, D.J., Farrell, E.J., Li, B., 2012. Temporal and spatial variability of aeolian sand transport: Implications for field measurements. *Aeolian Research* 3, 379–387.
- Gillies, J.A., Etyemezian, V., Nikolich, G., Glick, R., Rowland, P., Pesce, T., Skinner, M., 2017. Effectiveness of an array of porous fences to reduce sand flux: Oceano Dunes, Oceano CA. *Journal of Wind Engineering & Industrial Aerodynamics* 168, 247–259.
- Guan, D.X., Zhong, Y., Jin, C.J., Wang, A.Z., Wu, J.B., Shi, T.T., Zhu, T.Y., 2009. Variation in wind speed and surface shear stress from open floor to porous parallel windbreaks: A wind tunnel study. *J. Geophys. Res.* 114, D15106.
- Hatanaka, K., Hotta, S., 1997. Finite Element Analysis of Air Flow Around Permeable Sand Fences. *Int. J. Numer. Meth. Fl.* 24, 1291–1306.
- Herrmann, H.J., Andrade Jr., J.S., Schatz, V., Sauermann, G., Parteli, E.J.R., 2005. Calculation of the separation streamlines of barchans and transverse dunes. *Physica A* 357, 44–49.
- Herrmann, H.J., Durán, O., Parteli, E.J.R., Schatz, V., 2008. Vegetation and induration as sand dunes stabilizers. *J. Coastal Res.* 24, 1357–1368.
- Herrmann, H.J., Roux, S., 1990. *Statistical models for the fracture of disordered media.* Elsevier Science Publishers B. V. (North-Holland).
- Jerolmack, D.J., Ewing, R.C., Falcini, F., Martin, R.L., Masteller, C., Phillips, C., Reitz, M.D., Buynevich, I., 2012. Internal boundary layer model for the evolution of desert dune fields. *Nature Geoscience* 5, 206–209.

- Klose, M., Shao, Y., 2012. Stochastic parameterization of dust emission and application to convective atmospheric conditions. *Atmospheric Chemistry and Physics* 12, 7309.
- Kok, J.F., Parteli, E.J.R., Michaels, T.I., Bou Karam, D., 2012. The physics of wind-blown sand and dust. *Reports on Progress in Physics* 75, 106901.
- Kroy, K., Sauermann, G., Herrmann, H.J., 2002. Minimal model for aeolian sand dunes. *Phys. Rev. E* 66, 031302.
- Launder, B.E., Spalding, D.B., 1974. The numerical computation of turbulent flows. *Comput. Method. Appl. M.* 3, 269–289.
- Lee, S.J., Kim, H.B., 1999. Laboratory measurements of velocity and turbulence field behind porous fences. *J. Wind Eng. Ind. Aerod.* 80, 311–326.
- Lee, S.J., Park, K.C., Park, C.W., 2002. Wind tunnel observations about the shelter effect of porous fences on the sand particle movements. *Atmos. Environ.* 36, 1453–1463.
- Lettau, K., Lettau, H.H., 1978. Experimental and micro-meteorological field studies of dune migration, in: *Exploring the World's Driest Climate (IES Report)*. Madison, WI: University of Wisconsin-Madison, Institute for Environmental Studies. volume 101, pp. 110–147.
- Li, B., Ellis, J.T., Sherman, D.J., 2014. Estimating the impact threshold for wind-blown sand. *Journal of Coastal Research* 70, 627–632.
- Li, B., Sherman, D.J., 2015. Aerodynamics and morphodynamics of sand fences: A review. *Aeolian Research* 17, 33–48.
- Lima, I.A., Araújo, A.D., Parteli, E.J.R., Andrade, J.S., Herrmann, H.J., 2017. Optimal array of sand fences. *Scientific Reports* 7, 45148.
- Liu, B., Qu, J., Zhang, W., Tan, L., Gao, Y., 2014. Numerical evaluation of the scale problem on the wind flow of a windbreak. *Scientific Reports* 4, 6619.

- Lu, H., Shao, Y., 1999. A new model for dust emission by saltation bombardment. *Journal Geophysical Research* 104, 16827–16842.
- Luna, M.C.M.M., Parteli, E.J.R., Durán, O., Herrmann, H.J., 2009. Modeling transverse dunes with vegetation. *Physica A* 388, 4205–4217.
- Luna, M.C.M.M., Parteli, E.J.R., Durán, O., Herrmann, H.J., 2011. Model for the genesis of coastal dune fields with vegetation. *Geomorphology* 129, 215–224.
- Luna, M.C.M.M., Parteli, E.J.R., Herrmann, H.J., 2012. Model for a dune field with an exposed water table. *Geomorphology* 159-160, 169–177.
- Melo, H.P.M., Parteli, E.J.R., Andrade, J.S., Herrmann, H.J., 2012. Linear stability analysis of transverse dunes. *Physica A* 391, 4606–4614.
- Michelsen, B., Strobl, S., Parteli, E.J.R., Pöschel, T., 2015. Two-dimensional airflow modeling underpredicts the wind velocity over dunes. *Scientific Reports* 5, 16572.
- Nordstrom, K.F., Jackson, N.L., Freestone, A.L., Korotky, K.H., Puleo, J.A., 2012. Effects of beach raking and sand fences on dune dimensions and morphology. *Geomorphology* 179, 106–115.
- Parteli, E.J.R., Andrade Jr., J.S., Herrmann, H.J., 2011. Transverse instability of dunes. *Phys. Rev. Lett.* 107, 188001.
- Parteli, E.J.R., da Silva, L.R., Andrade Jr., J.S., 2010. Self-organized percolation in multi-layered structures. *Journal of Statistical Mechanics: Theory and Experiment* , P03026.
- Parteli, E.J.R., Kroy, K., Tsoar, H., Andrade Jr., J.S., Pöschel, T., 2014. Morphodynamic modeling of aeolian dunes: Review and future plans. *The European Physical Journal Special Topics* 223, 2269–2283.

- Parteli, E.J.R., Schwämmle, V., Herrmann, H.J., Monteiro, L.H.U., Maia, L.P., 2006. Profile measurement and simulation of a transverse dune field in the lençóis maranhenses. *Geomorphology* 81, 29–42.
- Patankar, S.V., Spalding, D.B., 1972. A calculation procedure for heat, mass and momentum transfer in three-dimensional parabolic flows. *Int. J. Heat Mass Transfer* 15, 1787–1806.
- Pye, K., Tsoar, H., 1990. *Aeolian sand and sand dunes*. Uwin Hyman, London.
- Qiu, G.Y., Lee, I.B., Shimizu, H., Gao, Y., Ding, G., 2004. Principles of sand dune fixation with straw checkerboard technology and its effects on the environment. *J. Arid Environ.* 56, 449–464.
- Raupach, M.R., 1992. Drag and drag partition on rough surfaces. *Boundary-Layer-Meteorology* 60, 374–396.
- Santiago, J.L., Martín, F., Cuerva, A., Bezdeneznykh, N., Sanz-Andrés, A., 2007. Experimental and numerical study of wind flow behind windbreaks. *Atmos. Environ.* 41, 6406–6420.
- Sauermann, G., Andrade Jr., J.S., Maia, L.P., Costa, U.M.S., Araújo, A.D., Herrmann, H.J., 2003. Wind velocity and sand transport on a barchan dune. *Geomorphology* 54, 245–255.
- Sauermann, G., Kroy, K., Herrmann, H.J., 2001. A continuum saltation model for sand dunes. *Phys. Rev. E* 64, 31305.
- Savage, R.P., 1963. Experimental study of dune building with sand fences, in: *Coastal Engineering 1962, Proceedings of the 8th International Conference, Mexico City, Mexico.. American Society of Civil Engineers.*
- Shao, Y., 2001. A model for mineral dust emission. *Journal of Geophysical Research* 106, 20239–20254.
- Shao, Y., 2008. *Physics and modelling of wind erosion*. Springer Science & Business Media.

- Shao, Y., Li, A., 1999. Numerical modelling of saltation in the atmospheric surface layer. *Boundary-Layer Meteorology* 91, 199–225.
- Shao, Y., Raupach, M.R., Findlater, P.A., 1993. Effect of saltation bombardment on the entrainment of dust by wind. *J. Geophys. Res.* 12, 12,719–12,726.
- Shao, Y., Yang, Y., 2005. A scheme for drag partition over rough surfaces. *Atmospheric Environment* 39, 7351–7361.
- Sherman, D.J., Li, B., Ellis, J.T., Farrell, E.J., Maia, L.P., Granja, H., 2013. Recalibrating aeolian sand transport models. *Earth Surf. Proc. Landforms* 38, 169–178.
- Stauffer, D., Aharony, A., 1994. *Introduction to Percolation Theory*. CRC Press, London.
- Telenta, M., Duhovnik, J., Kosel, F., Šajin, V., 2014. Numerical and experimental study of the flow through a geometrically accurate porous wind barrier model. *J. Wind Eng. Ind. Aerodyn.* 124, 99–108.
- Tsukahara, T., Sakamoto, Y., Aoshima, D., Yamamoto, M., Kawaguchi, Y., 2012. Visualization and laser measurements on the flow field and sand movement on sand dunes with porous fences. *Exp. Fluids* 52, 877–890.
- Wilson, J.D., 1985. Numerical studies of flow through a windbreak. *J. Wind Eng. Ind. Aerod.* 21, 119–154.
- Wilson, J.D., 1987. On the choice of a windbreak porosity profile. *Boundary-Lay. Meteorol.* 38, 37–49.
- Wilson, J.D., 2004. Oblique, Stratified Winds about a Shelter Fence. Part II: Comparison of Measurements with Numerical Models. *J. Appl. Meteorol.* 43, 1392–1409.
- Wu, X., Zou, X., Zhang, C., Wang, R., Zhao, J., Zhang, J., 2013. The effect of wind barriers on airflow in a wind tunnel. *Journal of Arid Environments* 97, 73–83.

- Yang, Y., Shao, Y., 2006. A scheme for scalar exchange in the urban boundary layer. *Boundary-Layer-Meteorology* 120, 111–132.
- Yeh, C.P., Tsai, C.H., Yang, R.J., 2010. An investigation into the sheltering performance of porous windbreaks under various wind directions. *J. Wind Eng. Ind. Aerodyn.* 98, 520–532.
- Zhang, N., Lee, S.J., Chen, T.G., 2015. Trajectories of saltating sand particles behind a porous fence. *Geomorphology* 228, 608–616.